Editors' Suggestion

Giant Dampinglike-Torque Efficiency in Naturally Oxidized Polycrystalline TaAs Thin Films

Wilson Yanez,[1] Yongxi Ou,[1] Run Xiao,[1] Supriya Ghosh,[2] Jyotirmay Dwivedi,[1] Emma Steinebronn,[1] Anthony Richardella,[1] K. Andre Mkhoyan,[2] and Nitin Samarth[1,*]

[1] *Department of Physics, Pennsylvania State University, University Park, Pennsylvania 16802, USA*
[2] *Department of Chemical Engineering and Materials Science, University of Minnesota, Minneapolis, Minnesota 55455, USA*

(Received 21 February 2022; revised 22 September 2022; accepted 29 September 2022; published 2 November 2022)

We report the measurement of efficient charge-to-spin conversion at room temperature in Weyl semimetal-ferromagnet heterostructures with both oxidized and pristine interfaces. Polycrystalline films of the Weyl semimetal, TaAs, are grown by molecular beam epitaxy on (001) GaAs and interfaced with a metallic ferromagnet ($Ni_{0.8}Fe_{0.2}$). Spin-torque ferromagnetic resonance (ST FMR) measurements yield a spin-torque ratio as large as $\xi_{FMR} = 0.45 \pm 0.25$ in samples with an oxidized interface. By studying ST FMR in these samples with varying $Ni_{0.8}Fe_{0.2}$ layer thickness, we find that the dampinglike-torque efficiency is $\xi_{DL} = 1.36 \pm 0.66$. In samples with a pristine (unoxidized) interface, the spin-torque ratio is $\xi_{FMR} = -0.27 \pm 0.14$ and has opposite sign to that observed in oxidized samples. We also find a lower bound on the spin Hall conductivity ($424 \pm 110\hbar/e$ S/cm), which is surprisingly consistent with theoretical predictions for the single-crystal Weyl semimetal state of TaAs.

DOI: 10.1103/PhysRevApplied.18.054004

The electrical manipulation of the spin degree of freedom in a material is a fundamental scientific aim that has a direct impact on nonvolatile, low dissipation magnetic memory applications. In this context, heavy metals and topological insulators have proven to be attractive platforms to study charge-spin interconversion due to the presence of significant spin Hall and Rashba-Edelstein effects [1–9]. More recently, Dirac and Weyl semimetals have started attracting interest for spintronics because of the potential for combining topological aspects of the band structure with increased electrical conductivity [10–16]. In particular, TaAs is an archetypal topological Weyl semimetal of contemporary interest [17] that has spin polarized surface states [18]. Although it is theoretically predicted to have a giant intrinsic spin Hall conductivity [19], this has yet to be demonstrated experimentally. Additionally, the role of natural oxidation has usually been neglected in topological materials, even though it has been shown that it can enhance the charge-spin interconversion efficiency in heavy metals and Dirac semimetals [13,20,21]. Several mechanisms have been proposed to explain this phenomenon, such as the presence of Rashba spin textures at the interface [22–24] or a theoretically predicted giant orbital Hall effect that can be further enhanced in oxide interfaces [25,26].

In this paper, we report measurements of the charge-spin interconversion phenomenon in polycrystalline thin films of TaAs interfaced with a metallic ferromagnet ($Ni_{0.8}Fe_{0.2}$) with and without natural surface oxidation. We show that at room temperature, the spin-torque ratio (also called spin-torque efficiency) in oxidized TaAs films can be as large as $\xi_{FMR} = 0.45 \pm 0.25$. We also present measurements of a completely *in vacuo* grown $TaAs/Ni_{80}Fe_{20}$ heterostructure, obtaining a spin-torque ratio $\xi_{FMR} = -0.27 \pm 0.14$ with a spin Hall conductivity that agrees quantitatively with prior *ab initio* calculations for the Weyl semimetal phase of TaAs [19]. This is surprising since the films measured here are polycrystalline. Notably, the sign of the spin-torque ratio is opposite for pristine versus oxidized samples since the sign of the symmetric component of the ST FMR spectra changes with oxidation. We then present a systematic study of the spin-torque ratio in oxidized TaAs samples as a function of the ferromagnet thickness and observe the presence of a significant fieldlike torque. Finally, we show that the sign change of the the spin-torque ratio also occurs when in simple metal $Ta/Ni_{0.8}Fe_{0.2}$ heterostructures when comparing oxidized and pristine interfaces.

We first discuss the synthesis of polycrystalline TaAs thin films using molecular beam epitaxy (MBE). TaAs crystallizes in a body-centered tetragonal structure ($I4_1md$ space group) with a lattice constant of $a = 0.3437$ nm and $c = 1.1656$ nm [17,18]. This makes it challenging to find

*nsamarth@psu.edu

an appropriate substrate for its thin-film epitaxial growth given that most commonly available semiconductors do not have lattice constants in this range [27]. We note that MBE growth of thin films of the related Weyl semimetals, NbP and TaP, has been reported using a thin Nb buffer layer on (001) MgO [28]. We try different substrates and find that GaAs (001) has the correct surface chemistry to nucleate TaAs growth. We carry out the synthesis in a VEECO 930 MBE chamber, monitoring the sample with reflection high-energy electron diffraction (RHEED) at 12 keV. After desorbing the native oxide on an epiready semi-insulating (001) GaAs substrate, we grow 30 nm of GaAs at a thermocouple temperature of 720 °C using Ga (5N) and As (5N) evaporated from different uncracked effusion cells. The Ga (As) beam equivalent pressure is 5×10^{-8} (7×10^{-7}) torr. We then cool down the substrate to a thermocouple temperature of 400 °C in the presence of As flux. At this point, we observe a RHEED pattern showing a 2×4 GaAs surface reconstruction [Fig. 1 (a)]. We then increase the temperature to 700–800 °C and conjointly deposited As and Ta (the latter from a four-pocket e-beam evaporator), obtaining the RHEED pattern shown in Fig. 1(b), which displays characteristics of the polycrystalline nature of the TaAs thin film (see Appendix A for details). We then transfer the TaAs films to an external electron-beam evaporator for the deposition of $Ni_{0.8}Fe_{0.2}$. Most of the samples studied here are transferred with a brief exposure to ambient, leading to an oxidized interface between TaAs and $Ni_{0.8}Fe_{0.2}$. A few samples are transferred using a vacuum suitcase enabling the study of TaAs/$Ni_{0.8}Fe_{0.2}$ heterostructures with a pristine interface. The complexity of the transfer procedure currently prevents us from doing a systematic study of unoxidized TaAs/$Ni_{0.8}Fe_{0.2}$ heterostructures as a function of $Ni_{0.8}Fe_{0.2}$ or TaAs layer thickness. The thickness of the $Ni_{0.8}Fe_{0.2}$ is controlled by a quartz crystal monitor during growth, and the deposition rate of each layer is then confirmed *ex situ* using x-ray reflectivity measurements. We also grow simple metal Ta/$Ni_{0.8}Fe_{0.2}$ heterostructures with and without natural oxidation on SiO_2 substrates using electron-beam evaporation for further spin-torque analysis. All samples used in ST FMR experiments are capped with 3 nm of Al to prevent oxidation of the $Ni_{0.8}Fe_{0.2}$ layer. Our past studies show self-limited oxidation of such Al layers [13].

We study the structural quality and crystalline phase of the TaAs films using x-ray diffraction. Figure 1(c) shows a $2\theta - \omega$ scan of a TaAs film, revealing (004), (008), and (112) peaks corresponding to the body-centered tetragonal phase of TaAs. Measurements of the rocking curve around the (004) peak show a full width half maximum angle of 0.73°. A reciprocal space map around the TaAs (004) peak displays isotropic broadening, consistent with the polycrystalline nature of the film [Fig. 1(d)]. Figure 1(e) shows the surface morphology of the film measured using atomic force microscopy (AFM). We observe several grains with a size of up to 100×50 nm^2. Height profiles of the AFM data in the vertical direction [Fig. 1(f)] show 1-nm height variations between different grains that match the lattice constant of TaAs along the *c* axis [17,18]. We also use electrical measurements in 10-nm- and 30-nm-thick TaAs films using a 1×0.5 mm^2 Hall-bar configuration and determine a resistivity in the range 124 to 318 $\mu\Omega$ cm. These values are 2 to 5 times larger than the values reported in bulk crystals of TaAs [29]. Magnetoresistance measurements at low temperature ($T = 2$ K) show signs of weak localization and Hall-effect measurements yield carrier densities on the order of 10^{21}–10^{22} cm^{-3} (see Appendix).

To obtain a deeper understanding of the microscopic structure of the TaAs thin films, we performed high-angle annular dark-field scanning transmission electron microscopy (HAADF STEM). Figure 2(a) shows a lower magnification image of the film cross-section having neighboring crystalline regions of different orientations, corresponding to the grains of TaAs about 5–10 nm in size. This can be better appreciated by taking the Fourier transform of smaller sections of the film showing unique crystal orientations, in order to identify the grain-boundary regions as shown in Fig. 2(b). The polycrystalline nature of the TaAs film grown can possibly result from the large lattice mismatch between TaAs and GaAs, 17.5% in the $\langle 100 \rangle$ direction and 16.5% in the $\langle 110 \rangle$ direction. To obtain the chemical composition information from the film, we use energy dispersive x-ray (EDX) spectroscopy in the TEM measurements [Fig. 2(c)]. Elemental distribution across the heterostructure showed a 1:1 stoichiometry between Ta and As in the film region [Fig. 2(d)]. Additionally, the 2-nm region of darker contrast seen in the HAADF images corresponds to the presence of an oxide layer of $TaAsO_x$, on the film surface also seen in the elemental maps. This is produced by the air exposure of the sample between the growth and its measurement (see Appendix F). This is further confirmed by x-ray spectroscopy from the surface of the film with take-off angles of 30° and 80° with respect to the sample surface plane. The spectra reveals the presence of Ta, As, Ta_2O_5, and AsO_x on its surface (see Appendix C).

We now discuss measurements of charge-spin conversion using ST FMR, focusing on the naturally oxidized TaAs/$Ni_{0.8}Fe_{0.2}$ heterostructures. We use standard lithography techniques to pattern the films into 50×10 μm^2 bars and deposited Ti/Au contacts for electrical measurement [Fig. 3(a)]. We measure a total of 16 devices including TaAs and Ta films with and without natural oxidation of its surface before the $Ni_{0.8}Fe_{0.2}$ deposition. Amongst these, we include the data of one TaAs film with a pristine surface. All the ST FMR measurements involving TaAs are performed in 10-nm-thick films. At this thickness, we can neglect possible spin-pumping contributions

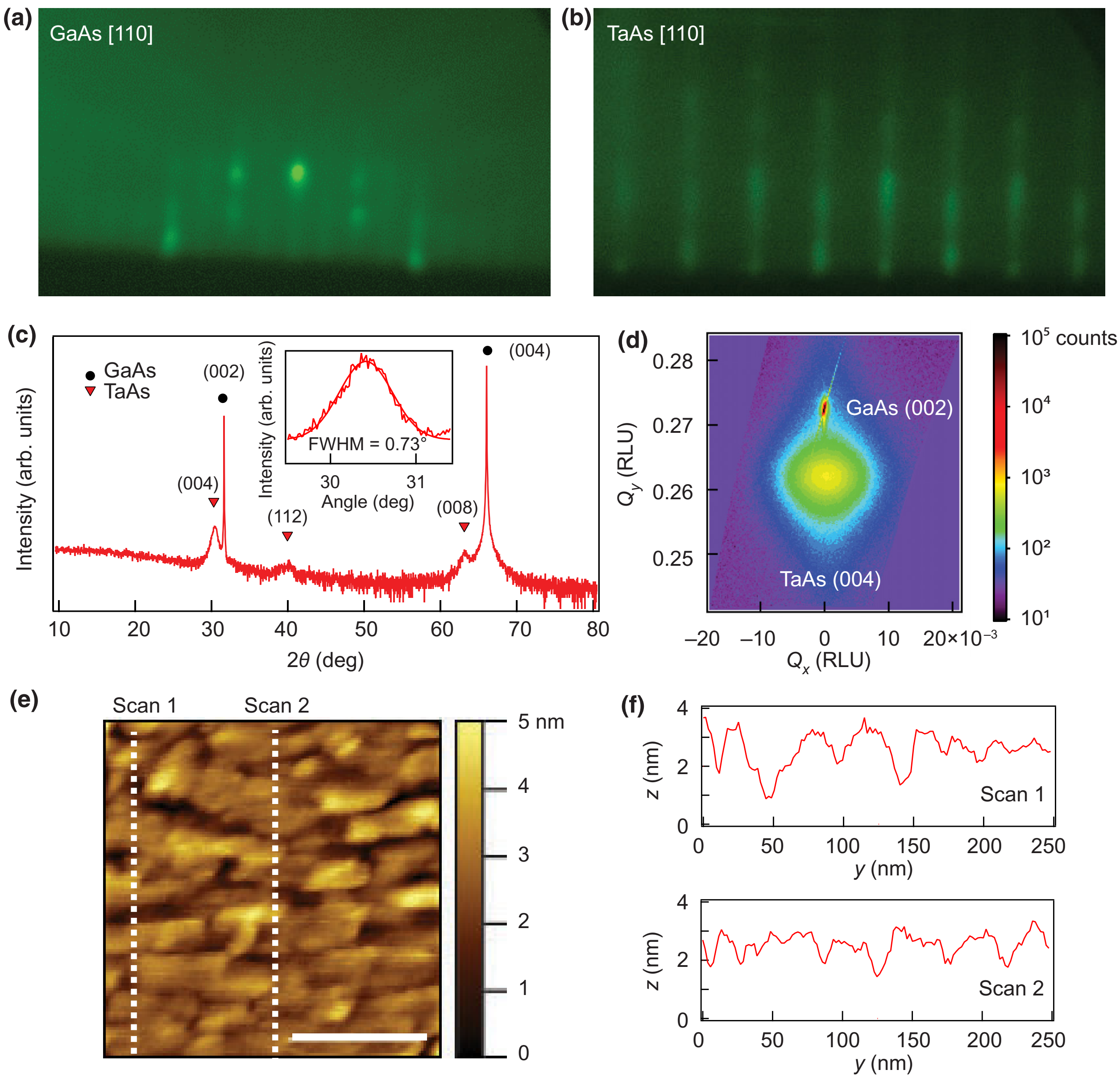

FIG. 1. RHEED pattern of the GaAs (a) and TaAs (b) layers along the [110] GaAs crystal direction. (c) X-ray diffraction 2θ scan of a 30-nm-thick TaAs film. The inset shows the rocking curve of the (004) TaAs peak, showing a full width half maximum of 0.73°. (d) Reciprocal space map of the TaAs thin film around the (004) peak in relative lattice units (RLUs). (e) AFM image of the TaAs surface with a 100-nm scale bar. (f) Height profiles along the vertical directions shown in (e) of the TaAs film.

in the measured signal due to the inverse Hall effect that has been reported in other semimetals at thicknesses higher than 10 nm [30,31]. To perform the ST FMR experiments [Fig. 3(b)], we apply a radio-frequency charge current (J_c) along the heterostructure, which produces a flow of angular momentum (spin current, J_s) in a direction perpendicular to the flow of charge via the spin Hall or Rashba-Edelstein effects. The spin accumulation in the TaAs/$Ni_{0.8}Fe_{0.2}$ interface, after being absorbed into the ferromagnet, applies a torque on its magnetization causing it to precess. This phenomenon can then be measured as a rectified voltage across the device (V_{mix}) due to the mixing of the applied current and the anisotropic magnetoresistance of the ferromagnet [2] (see Appendix D). This allows us to obtain the spectra shown in Figs. 3(c) and 3(d). In addition to the spin-generated torques, the flow of charge also produces an Oersted field that interacts with the magnetization and produces an out-of-plane torque that can be used to quantify the spin-torque ratio [2,3]. We fit the resonance spectrum with a symmetric and antisymmetric Lorentzian contribution and determine the spin-torque ratio, which is given by

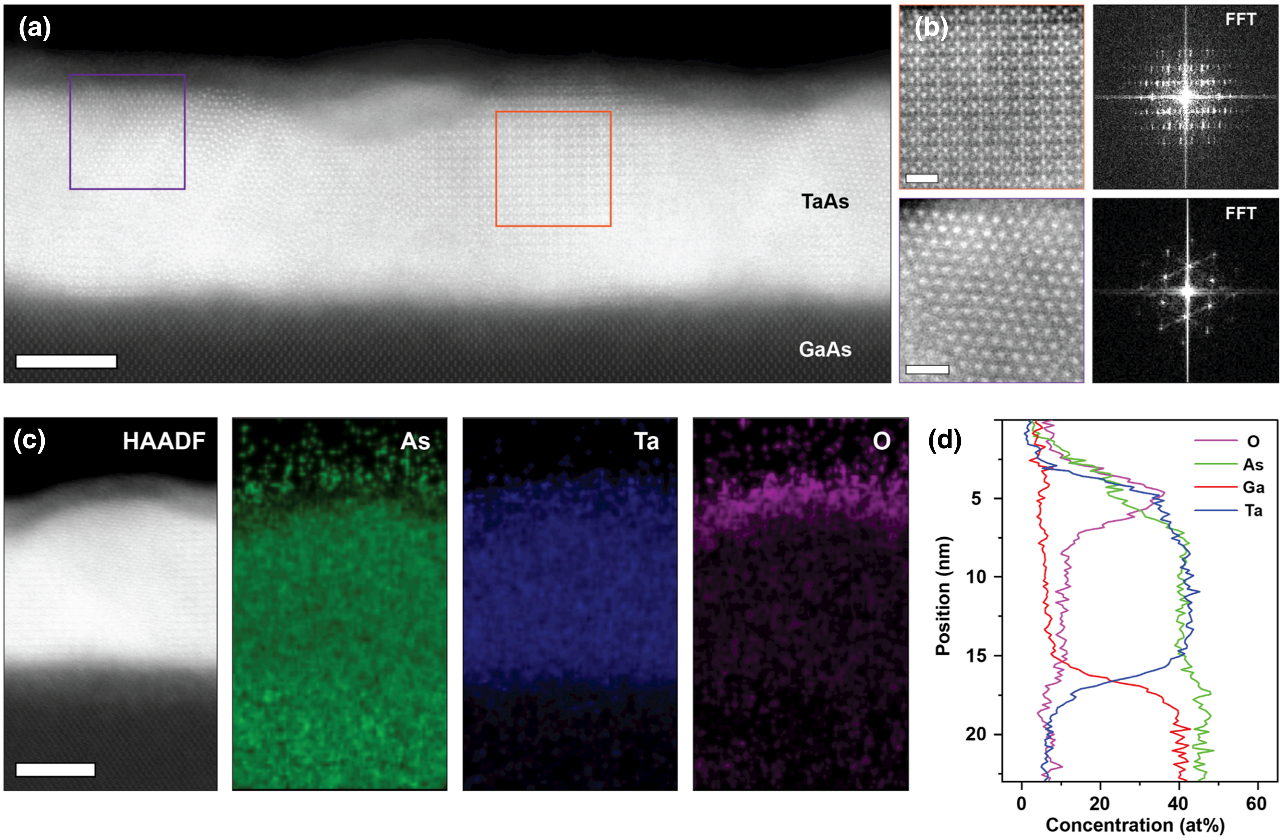

FIG. 2. (a) HAADF STEM image of the heterostructure cross section showing an approximately 10-nm polycrystalline TaAs film grown on the GaAs layer. Scale bar is 5 nm. (b) Higher magnification STEM images of regions highlighted in (a) with their corresponding fast Fourier transforms (FFTs), showing the different grains present in the polycrystalline TaAs film layer highlighted in (a). Scale bars are 1 nm. (c) Elemental maps of As, Ta, and O, showing the distribution of these elements across the film interface. Scale bar is 5 nm. (d) Concentration (atomic percent) of the Ta, Ga, As, and O elements across the thin-film section obtained from STEM EDX.

[2,4,13]

$$\xi_{\mathrm{FMR}} = \frac{S}{A}\left(\frac{e}{\hbar}\right)\mu_0 M_S t_{\mathrm{TaAs}} t_{\mathrm{NiFe}}\left[1+\left(\frac{M_{\mathrm{eff}}}{H_{\mathrm{res}}}\right)\right]^{1/2}. \quad (1)$$

Here, ξ_{FMR} is the spin-torque ratio, S (A) is the amplitude of the symmetric (antisymmetric) Lorentzian fit, e is the charge of the electron, $\hbar$ is the reduced Planck constant, μ_0 is the permeability of free space, $M_S = 560$ kA/m is the saturation magnetization of $\mathrm{Ni_{0.8}Fe_{0.2}}$ measured in a superconducting quantum interference device magnetometer, t_{TaAs} is the thickness of the TaAs layer, t_{NiFe} is the thickness of the ferromagnet, M_{eff} is the effective magnetization obtained from fitting the Kittel FMR equation to the spectra and H_{res} is the magnitude of magnetic field at which the resonance happens.

If the symmetric signal is produced solely by spin torque (in-plane) while the antisymmetric signal is produced by a combination of spin torque, Oersted field and other current-induced effective field-like torques (out-of-plane), we can write Eq. (1) as [3]:

$$\frac{1}{\xi_{\mathrm{FMR}}} = \frac{1}{\xi_{\mathrm{DL}}}\left(1+\frac{\hbar}{e}\frac{\xi_{\mathrm{FL}}}{\mu_0 M_S t_{\mathrm{TaAs}} t_{\mathrm{NiFe}}}\right). \quad (2)$$

Here, $\xi_{\mathrm{DL(FL)}} = (2e/\hbar)(4\pi M_S t_{\mathrm{NiFe}})(H_{\mathrm{OP(IP)}}/J_c)$ is the efficiency of the in-plane, dampinglike (out-of-plane, fieldlike) torques, defined as the normalized ratio of the field $H_{\mathrm{OP(IP)}}$ generated in the out-of-plane (in-plane) directions to the charge current flowing in the device [3]. In systems where the current-induced effective fieldlike torque is negligible, the spin-torque ratio is equal to the dampinglike torque efficiency ($\xi_{\mathrm{FMR}} = \xi_{\mathrm{DL}}$).

First, we focus on the naturally oxidized samples (abbreviated as TaAsO_x in the rest of this work). In Fig. 3(c), we observe the spectra of a 10-nm oxidized TaAs film with an 8-nm $\mathrm{Ni_{0.8}Fe_{0.2}}$ layer. When we fit the data, we see a large symmetric component in the spectrum (V_{DL}) that is larger than the antisymmetric one (V_{FL}) and has the same sign as platinum control samples (not shown). We extract the spin-torque ratio of this heterostructure using Eq. (1) and

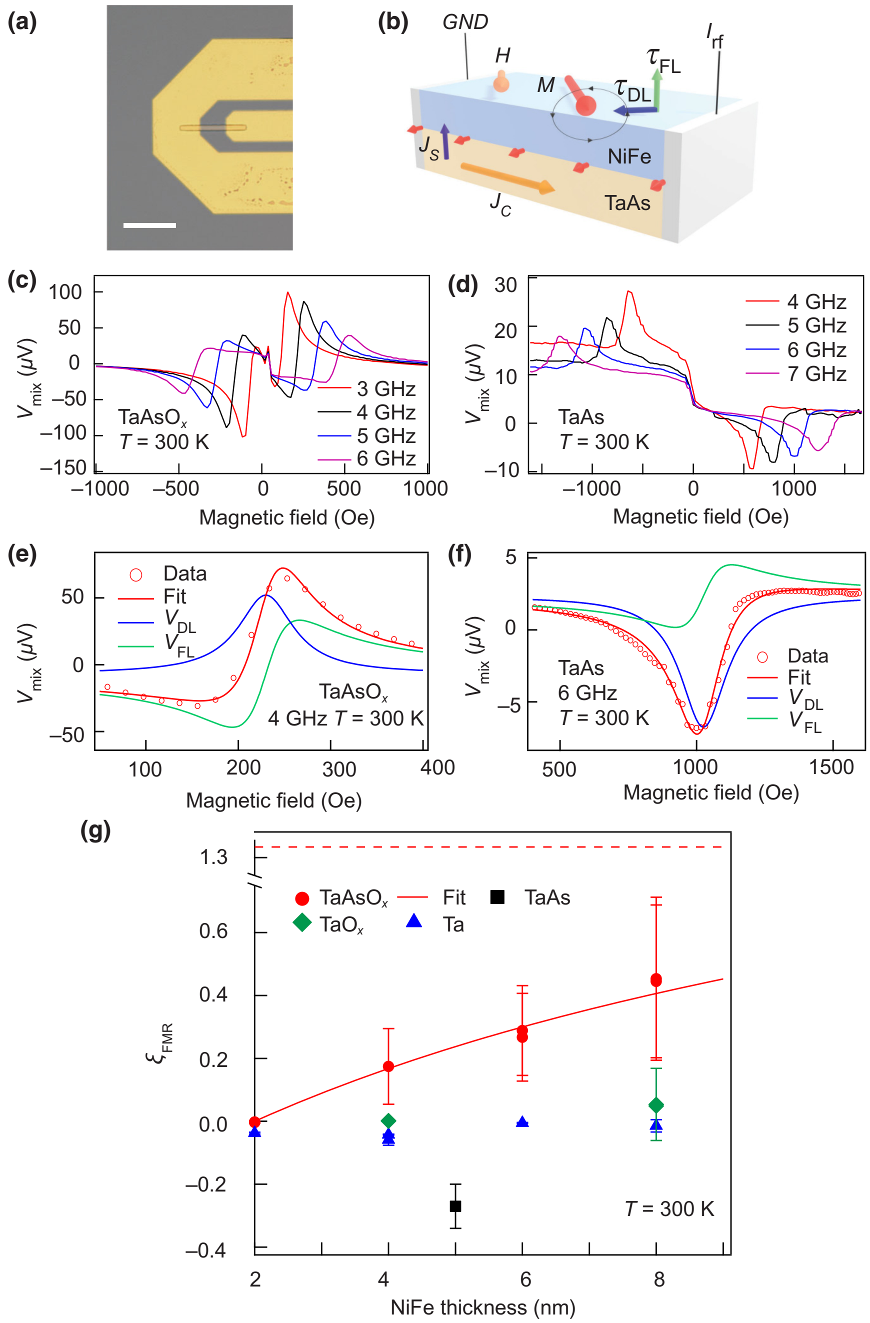

FIG. 3. (a) Optical image of a device used for ST FMR measurements. The scale bar represents 100 μm. (b) Schematic of the charge-to-spin conversion process in TaAs/$Ni_{0.8}Fe_{0.2}$ heterostructures. Room-temperature ST FMR spectra measured at different excitation frequencies of (c) a 10-nm naturally oxidized TaAs polycrystalline film with 8 nm of $Ni_{0.8}Fe_{0.2}$ and (d) a nonoxidized 10-nm TaAs polycrystalline film with 5 nm of $Ni_{0.8}Fe_{0.2}$ (d). Fitted data of (e) the oxidized and (f) nonoxidized samples described in (c) and (d), respectively. These show the dampinglike symmetric (V_{DL}) and fieldlike antisymmetric (V_{FL}) Lorentzian contributions used in the fit. (g) Spin-torque ratio of TaAs and Ta with and without natural oxidation as a function of $Ni_{0.8}Fe_{0.2}$ thickness. The solid line shows the fit of the TaAsO$_x$ data and the dashed line its saturation value.

obtain $\xi_{FMR} = 0.45 \pm 0.25$. For further insight into the origin of this large spin-torque ratio, we grow a set of samples with fixed TaAs thickness (10 nm) and different $Ni_{0.8}Fe_{0.2}$ thickness. We compute the spin-torque ratio of each sample and observe that it monotonically increases with the thickness of the ferromagnet [Fig. 3(g)]. This indicates the presence of a significant current-induced positive fieldlike torque [32] and a giant dampinglike torque with an efficiency higher than our largest experimental value (see Appendix E). To quantify this phenomenon, we perform a linear fit of the inverse spin-torque ratio as a function of the inverse ferromagnet thickness considering a 2-nm dead layer in the ferromagnet and use Eq. (2) to determine the dampinglike and fieldlike torque efficiencies. These values are $\xi_{DL} = 1.36 \pm 0.66$ and $\xi_{FL} = 0.30 \pm 0.15$ (see Appendix E). The linear behavior of the data used for the regression suggests that the spin-pumping effect is negligible in these samples [31]. At present, we cannot determine the spin Hall conductivity of oxidized TaAs due to the difficulty of precisely determining the electrical conductivity of $TaAsO_x$. Nevertheless, the value of the dampinglike and fieldlike torque efficiency is comparable to that measured in topological insulators (Bi_2Se_3) [4,5,33] and higher than heavy metals (Pt, Ta) [3,34,35], Weyl semimetals (WTe_2) [36], Dirac semimetals (Cd_3As_2)[13], and Dirac nodal-line semimetals (IrO_2) [34].

Next we focus on the pristine (unoxidized) TaAs/$Ni_{0.8}Fe_{0.2}$ heterostructure. Figure 3(f) shows that the symmetric component of the spectra changes sign with respect to the one taken in oxidized samples [Fig. 3(e)]. We follow the same procedure described above and obtain the spin-torque ratio of nonoxidized TaAs $\xi_{FMR} = -0.27 \pm 0.07$. The sign of the spin-torque ratio is opposite to naturally oxidized TaAs and Pt control samples (see Appendix D). Assuming the effective fieldlike torque is negligible in the pristine TaAs sample, this sets a lower bound on the spin Hall angle (θ_{SH}) due to the less than ideal spin transparency of the $Ni_{0.8}Fe_{0.2}$ interface ($\theta_{SH} \geq \xi_{FMR}$) [3]. The spin-torque ratio can then be combined with our electrical conductivity measurements to obtain the spin Hall conductivity of TaAs. We find that in TaAs the lowest value of electrical conductivity measured in a Hall-bar configuration is ($\sigma_{xx} = 3144$ S cm^{-1}), which implies that $|\sigma_{SH}| = (\hbar/2e)|\theta_{SH}|\sigma_{xx} \gtrsim 424 \pm 110$ $(\hbar/e)$ (S/cm). This experimental value agrees with the theoretical prediction of a negative giant spin Hall conductivity in TaAs [19]. We notice that the theoretical spin Hall conductivity of TaAs strongly depends on the position of the chemical potential in the film. Sample variation, the polycrystalline nature of our films, and a possible band-bending effect due to the adjacent ferromagnet makes it challenging to relate the measured and theoretical quantities. Nevertheless this value seems to quantitatively agree with the first-principles calculation near the Fermi level [19].

To study the effect of the oxide on the giant damping like spin-torque ratio measured in TaAs films, we measure the ST FMR spectra of simple metal Ta/$Ni_{0.8}Fe_{0.2}$ heterostructures evaporated on SiO_2 with and without natural oxidation. We kept the Ta layer fixed at 6 nm, varied the $Ni_{0.8}Fe_{0.2}$ thickness, and computed the spin-torque ratio of each device [Fig. 3(f)]. Even though there is variation among samples due to the lack of precise control over the oxide layer, we find that oxidation at the interface changes the sign of the spin-torque ratio: it is positive in naturally oxidized Ta ($TaO_x/Ni_{0.8}Fe_{0.2}$) ($\xi_{FMR} = 0.037 \pm 0.030$) while it is negative in nonoxidized Ta/$Ni_{0.8}Fe_{0.2}$ heterostrucures ($\xi_{FMR} = -0.032 \pm 0.009$). These values are one order of magnitude smaller than the ones measured in TaAs; thus, the oxide itself cannot alone explain the large spin-torque ratio measured in TaAs. Nevertheless, this comparison with control Ta layers show once again our qualitative finding that the presence of oxide can change the sign of the symmetric component in the ST FMR spectrum.

In conclusion, we demonstrate that it is possible to deposit thin films of TaAs on GaAs in a way that is compatible with standard III-V semiconductor processing. This allows us to experimentally measure a giant spin-torque ratio in naturally oxidized and pristine polycrystalline TaAs/$Ni_{0.8}Fe_{0.2}$ heterostructures. We observe the presence of large dampinglike and fieldlike torques with efficiencies that are greater in magnitude than other materials of contemporary interest [3–5,13,33–36]. The extracted spin Hall conductivity of pristine TaAs is in remarkable agreement with theoretical predictions [19]. We show that the presence of an oxide produces a positive damping-like torque efficiency that changes the sign of the symmetric component of the ST-FMR spectrum. We show that the electronic states of this oxide layer located in the surface of the film can be spin polarized and could easily be confused with a topological surface state. For this reason our work calls for caution while claiming topological behavior in oxidized materials. Several mechanisms have been identified as possible ways to produce spin torques due to oxidation, including enhanced spin Hall and Rashba-Edelstein effects [13,20], material-dependent electron distribution near interfaces [21], and an oxide-enhanced giant orbital Hall effect in transition metals [25,26]. The polycrystalline nature of our films may possibly also enhance the spin-torque ratio due to quantum confinement effects, akin to observations in topological insulators [37], but this is only speculation at present. The topological Weyl semimetal nature of TaAs with spin-polarized surface states also likely plays a key role in enhancing the intrinsic spin Hall conductivity [19]. Determining and separating each of these contributions requires a higher control of the heterostructure that goes beyond the scope of this work. Nevertheless, our observation of a sign change in the ST FMR spectra in oxidized samples is an easy and immediate way to discriminate between intrinsic effects and effects due to oxidation. The large spin-torque efficiencies demonstrated in TaAs have an immediate impact for fundamental research on spin-related phenomena in topological materials and in technological spintronic applications.

ACKNOWLEDGMENTS

The authors would like to thank D.C. Ralph for valuable comments and A. Sengupta for providing access to apparatus used in ST FMR measurements. The principal support for this project is provided by SMART, one of seven centers of nCORE, a Semiconductor Research Corporation program, sponsored by the National Institute of Standards and Technology (NIST). This supported the synthesis and standard characterization of TaAs heterostructures as well as charge-spin conversion measurements (W.Y., Y.O., J.D., N.S.) and their characterization using STEM (S.G., A.M.). Additional support for materials synthesis and characterization was provided by the Penn State Two-Dimensional Crystal Consortium-Materials Innovation Platform (2DCC-MIP) under NSF Grant No. DMR-2039351 (R.X., E.S., A.R., N.S.). Parts of this work were carried out in the Characterization Facility, University of Minnesota, which receives partial support from the NSF through the MRSEC (Award No. DMR-2011401) and the NNCI (Award No. ECCS-2025124) programs.

APPENDIX A: GROWTH OF TaAs THIN FILMS AND RHEED PATTERNS ALONG DIFFERENT CRYSTAL DIRECTIONS

TaAs crystallizes in a body-centered tetragonal structure ($I4_1md$ space group) with a lattice constant of $a = 0.3437$ nm and $c = 1.1656$ nm [17,18]. This makes it especially challenging to find an appropriate substrate for the thin-film epitaxial growth of TaAs given that most commonly available semiconductors have lattice constants ranging from 0.541 to 0.648 nm [27]. We try to deposit TaAs in a variety of substrates including GaAs, MgO, $SrTiO_3$, GaSb, and $MgAl_2O_4$ with the hope of stabilizing the film in a crystal orientation different than (001). Nevertheless, none of these samples show a clear RHEED pattern except for the films grown on GaAs; this suggests that GaAs has the correct surface chemistry to nucleate TaAs growth. A second major obstacle in the synthesis of TaAs is the extremely high temperature (approximately 3000 °C) required for Ta evaporation. This cannot be achieved with a regular Knudsen effusion cell; if Ta is evaporated from a crucible in this temperature range, the vapor pressure of the crucible itself is significant enough to cause contamination in the sample. For these reasons, we evaporate Ta from 2- and 4-mm-diameter rods using a four-pocket electron-beam evaporator. To achieve a reasonable Ta deposition rate, we increase the power applied to the rod until it melts and forms a controlled molten drop on one end. This allow us to achieve growth rates as high as 2.5 nm/h for the 2-mm rod and 10 nm/h for the 4-mm rod.

In Fig. 4, we show the RHEED patterns of GaAs and TaAs films along different crystal directions. GaAs shows a 2×4 surface reconstruction. In TaAs, the separation between fringes changes continuously as we rotate the sample, indicating polycrystalline growth.

APPENDIX B: ELECTRICAL CHARACTERIZATION OF TaAs IN THE HALL-BAR CONFIGURATION

We used standard lithography techniques to pattern a 1×0.5 mm^2 Hall bar (Fig. 5) and measured its resistance and Hall effect as a function of temperature and magnetic field. The resistivity of the sample monotonically increases with increasing temperature consistent with the expected metallic behavior of TaAs [29]. The residual resistivity ratio is small, consistent with the disorder in the polycrystalline film. At low temperature ($T \lesssim 10$ K, the magnetoresistance shows holelike behavior with signatures of weak antilocalization. We compute the carrier density in the TaAs thin films using the Hall effect and obtain values on the order of 10^{21}–10^{22} cm^{-3}.

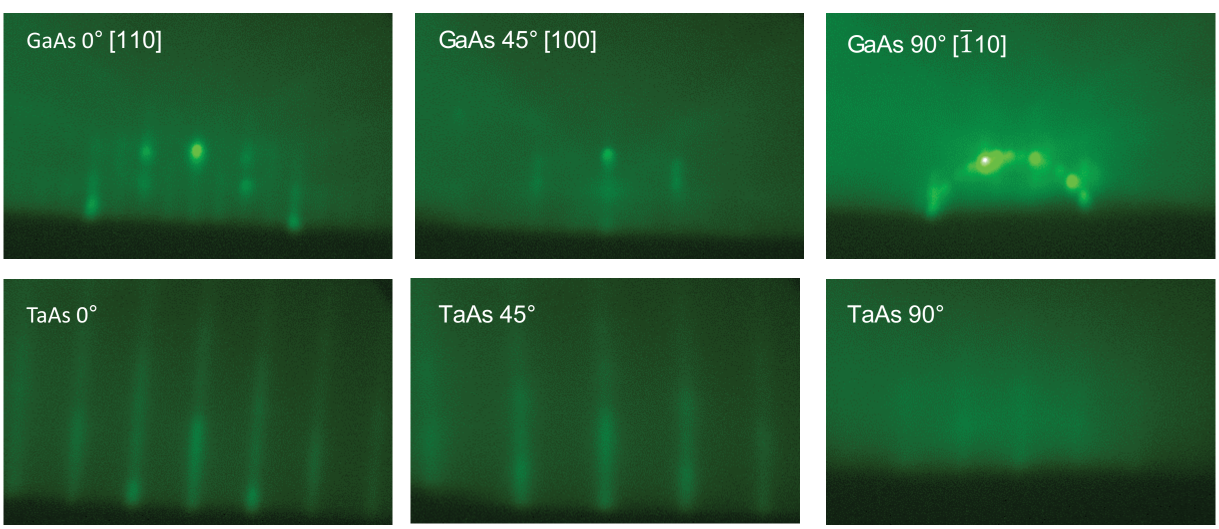

FIG. 4. RHEED patterns of GaAs and TaAs along different crystal directions.

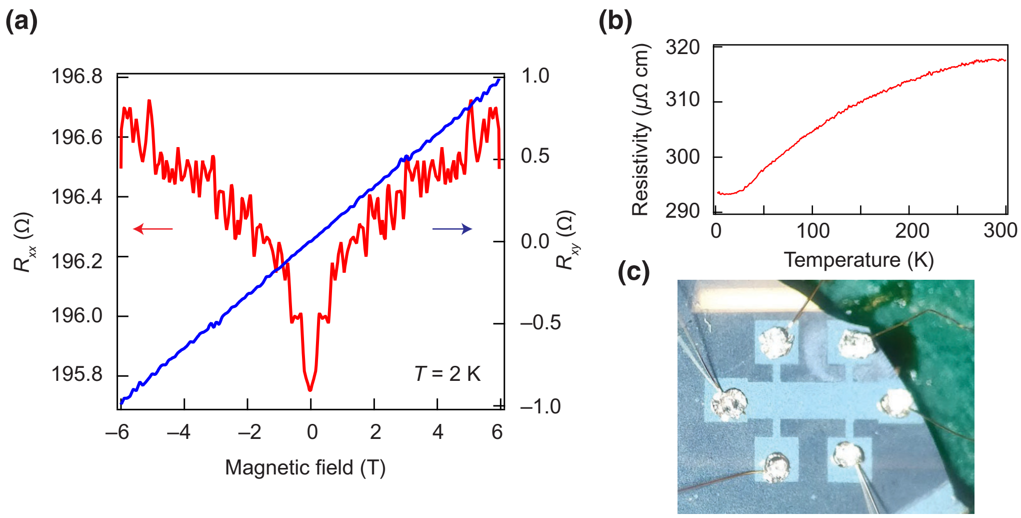

FIG. 5. (a) Longitudinal (R_{xx}) and transverse (R_{xy}) resistance as a function of magnetic field at $T = 2$ K in a 30-nm-thick TaAs film. (b) Resistivity of a 30-nm-thick TaAs film as a function of temperature. (c) Optical image of the Hall bar used in these measurements.

APPENDIX C: XPS DATA ON TaAs THIN FILMS

XPS experiments are performed on TaAs films of different thicknesses (Fig. 6) using a Physical Electronics VersaProbe II instrument equipped with a monochromatic Al $K\alpha$ x-ray source ($h\nu = 1486.7$ eV) and a concentric hemispherical analyzer. Charge neutralization is performed using both low-energy electrons (< 5 eV) and Ar ions. The binding energy axis is calibrated using sputter cleaned Cu (Cu $2p_{3/2} = 932.62$ eV, Cu $3p_{3/2} = 75.1$ eV) and Au foils (Au $4f_{7/2} = 83.96$ eV). Peaks are charge referenced to CH_x band in the carbon 1*s* spectra at 284.8 eV. Measurements are made at takeoff angles of 30° and 80° with respect to the sample surface plane. This results in a typical sampling depth of 2–3 nm and 4–6 nm, respectively (95% of the signal originated from this depth or shallower). Quantification is done using instrumental relative sensitivity factors that account for the x-ray cross section and inelastic mean free path of the electrons.

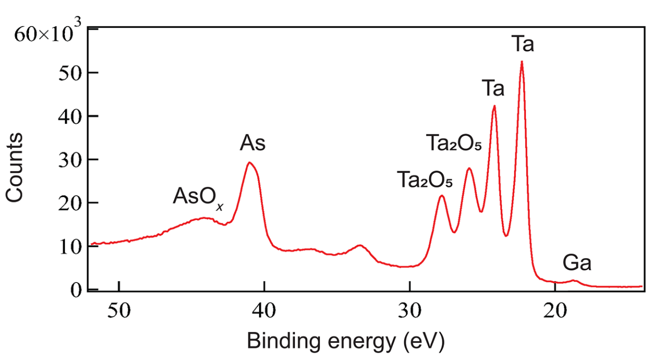

FIG. 6. XPS data taken on a 10-nm-thick oxidized TaAs film measured at 80° with respect to the sample surface plane indicating the presence of Ta_2O_5 and AsO_x.

APPENDIX D: ST FMR MEASUREMENTS OF OXIDIZED AND PRISTINE Ta AND TaAs

All the ST FMR measurements are performed at room temperature using a Keithley 2182 nanovoltmeter, a radiofrequency current of 2 to 7 GHz and an external magnetic field up to 1600 Oe. Figure 7 shows the ST FMR spectrum of oxidized and pristine TaAs and Ta films that have been interfaced with $Ni_{0.8}Fe_{0.2}$ films of different thickness. These signals are fitted using a symmetric and antisymmetric Lorentzian. The fieldlike antisymmetric contribution (V_{FL}) has the same sign in all the samples while the symmetric contribution (V_{DL}) changes sign in oxidized films in comparison with pristine ones. We also observe a large enhancement of spin-torque ratio in the pristine and oxidized TaAs films in comparison with pure Ta ones. This indicates that the spin-torque signal measured in $TaAsO_x$ cannot be explained by the presence of TaO_x alone.

APPENDIX E: ANALYSIS OF THE SPIN-TORQUE RATIO IN OXIDIZED TaAs SAMPLES WITH DIFFERENT FERROMAGNET THICKNESS

To separate the contributions of the dampinglike torque and other current-induced effective fieldlike torques in oxidized TaAs films [3], we grow a set of samples where we keep the thickness of the TaAs layer constant at 10 nm and vary the thickness of the ferromagnetic $Ni_{0.8}Fe_{0.2}$ layer. We notice that the spin-torque ratio is close to zero in samples with 2 nm of $Ni_{0.8}Fe_{0.2}$. Together with a noticeable roughness in the TaAs surface [Fig. 2(a) of the main text], this suggests the possible presence of an approximately 2-nm dead magnetic layer at the TaAs/$Ni_{0.8}Fe_{0.2}$ interface. To take this effect into account, we subtract the thickness of

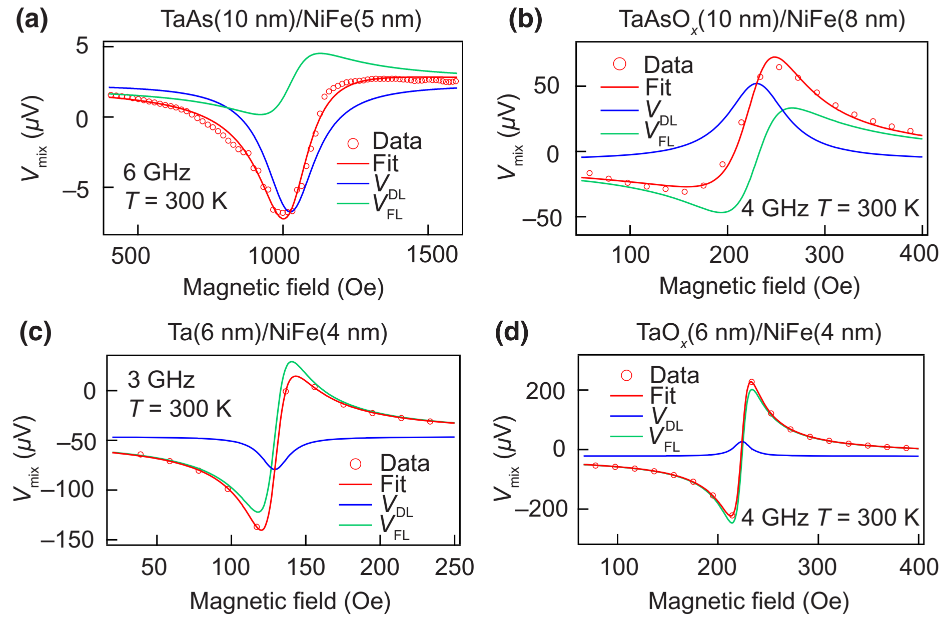

FIG. 7. Room-temperature ST FMR spectrum of pristine (a) and oxidized TaAs (b) and pristine (c) and oxidized (d) Ta. The figure shows the fitted data showing the dampinglike symmetric (V_{DL}) and fieldlike antisymmetric (V_{FL}) Lorentzian contributions used in the fit.

this dead layer from the $\mathrm{Ni_{0.8}Fe_{0.2}}$ thickness, as measured using a quartz crystal monitor during the deposition. This allows us to use Eq. (E1) [Eq. (2) in the main text] to determine the dampinglike and fieldlike torque efficiencies of oxidized TaAs.

$$\frac{1}{\xi_{\mathrm{FMR}}}=\frac{1}{\xi_{\mathrm{DL}}}\left(1+\frac{\hbar}{e}\frac{\xi_{\mathrm{FL}}}{\mu_0 M_S t_{\mathrm{TaAs}} t_{\mathrm{NiFe}}}\right). \tag{E1}$$

Here, ξ_{FMR} is the measured spin-torque ratio, $\xi_{\mathrm{DL(FL)}} = (2e/\hbar)(J_{s,\mathrm{DL(FL)}}/J_c)$ is the spin-torque efficiency of the in-plane, dampinglike (out-of-plane, fieldlike) torques defined as the ratio of the spin current generating each torque by the amount of charge current flowing in the device, e is the charge of the electron, $\hbar$ is the reduced Planck constant, μ_0 is the permeability of free space, $M_S = 560$ kA/m is the saturation magnetization of $\mathrm{Ni_{0.8}Fe_{0.2}}$, t_{TaAs} is the thickness of the TaAs layer, t_{NiFe} is the effective thickness of the ferromagnet after subtracting the dead-layer thickness (2 nm).

We perform a linear regression on the data shown in Fig. 8(a) and obtain the efficiencies to be $\xi_{\mathrm{DL}} = 1.36 \pm 0.66$ and $\xi_{\mathrm{FL}} = 0.30 \pm 0.15$. This indicates the presence of a significant positive current-induced fieldlike torque on this system and a giant dampinglike torque with an efficiency higher than our largest experimental value ($\xi_{\mathrm{FMR}} = 0.45$

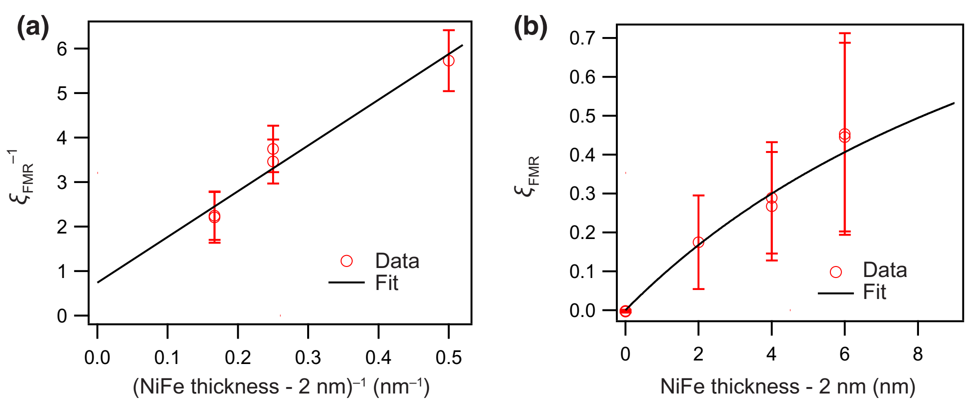

FIG. 8. (a) Inverse spin-torque ratio as a function of inverse $\mathrm{Ni_{0.8}Fe_{0.2}}$ thickness for oxidized TaAs films showing the data and its linear fit. (b) Spin-torque ratio as a function of $\mathrm{Ni_{0.8}Fe_{0.2}}$ thickness for the same sample as (a). The values for the fit are determined from (a). In both panels, we subtract 2 nm to the $\mathrm{Ni_{0.8}Fe_{0.2}}$ thickness to account for a possible ferromagnetic dead layer at the TaAs/$\mathrm{Ni_{0.8}Fe_{0.2}}$ interface.

with 8-nm $Ni_{0.8}Fe_{0.2}$. This can be seen better in Fig. 8(b), in which we use the parameters obtained from the linear fit to draw the nonlinear behavior of the spin-torque ratio as a function of ferromagnet thickness. We perform a similar analysis ignoring the presence of the ferromagnetic dead layer and obtain an unphysical negative dampinglike torque efficiency that does not agree with the positive dampinglike torque (symmetric component of the ST FMR spectra) measured in oxidized samples [Fig. 7(a)]. Moreover, the linear behavior of the data shows that other possible artifacts, like spin pumping due to the inverse spin Hall effect are not significant in the heterostructure [31].

APPENDIX F: STEM CHARACTERIZATION OF TaAs FILMS

Samples for cross-section STEM characterization are prepared on a FEI Helios Nanolab G4 dual-beam focused ion-beam (FIB) instrument. The sample is coated with amorphous carbon prior to sectioning, in order to prevent film-surface damage by the Ga ion beam. The sample is thinned first using a 30-keV Ga ion beam follow by 2 keV Ga ion beam to remove the damage surface layers. HAADF STEM imaging and STEM EDX spectroscopy are performed on an aberration-corrected FEI Titan G2 60–300 (S)TEM microscope, which is equipped with a CEOS DCOR probe corrector, a monochromator and a super-x-EDX spectrometer. The microscope is operated at 200 keV with a probe convergence angle of 25.5 mrad. The inner and outer collection angles used for the HAADF detector are 55 and 200 mrad, respectively. EDX maps are collected and analyzed using the Bruker Espirit 1.9 software.

[1] L. Liu, C.-F. Pai, Y. Li, H. W. Tseng, D. C. Ralph, and R. A. Buhrman, Spin-torque switching with the giant spin Hall effect of Tantalum, Science **336**, 555 (2012).

[2] L. Liu, T. Moriyama, D. C. Ralph, and R. A. Buhrman, Spin-Torque Ferromagnetic Resonance Induced by the Spin Hall Effect, Phys. Rev. Lett. **106**, 036601 (2011).

[3] C.-F. Pai, Y. Ou, L. H. Vilela-Leão, D. C. Ralph, and R. A. Buhrman, Dependence of the efficiency of spin Hall torque on the transparency of Pt/ferromagnetic layer interfaces, Phys. Rev. B **92**, 064426 (2015).

[4] A. R. Mellnik, J. S. Lee, A. Richardella, J. L. Grab, P. J. Mintun, M. H. Fischer, A. Vaezi, A. Manchon, E.-A. Kim, N. Samarth, and D. C. Ralph, Spin-transfer torque generated by a topological insulator, Nature **511**, 449 (2014).

[5] H. Wang, J. Kally, J. S. Lee, T. Liu, H. Chang, D. R. Hickey, K. A. Mkhoyan, M. Wu, A. Richardella, and N. Samarth, Surface-State-Dominated Spin-Charge Current Conversion in Topological-Insulator/Ferromagnetic-Insulator Heterostructures, Phys. Rev. Lett. **117**, 076601 (2016).

[6] H. Wang, J. Kally, C. Şahin, T. Liu, W. Yanez, E. J. Kamp, A. Richardella, M. Wu, M. E. Flatté, and N. Samarth, Fermi level dependent spin pumping from a magnetic insulator into a topological insulator, Phys. Rev. Res. **1**, 012014(R) (2019).

[7] Y. Wang, D. Zhu, Y. Wu, Y. Yang, J. Yu, R. Ramaswamy, R. Mishra, S. Shi, M. Elyasi, K.-L. Teo, Y. Wu, and H. Yang, Room temperature magnetization switching in topological insulator-ferromagnet heterostructures by spin-orbit torques, Nat. Commun. **8**, 1364 (2017).

[8] H. Wu, P. Zhang, P. Deng, Q. Lan, Q. Pan, S. A. Razavi, X. Che, L. Huang, B. Dai, K. Wong, X. Han, and K. L. Wang, Room-Temperature Spin-Orbit Torque from Topological Surface States, Phys. Rev. Lett. **123**, 207205 (2019).

[9] K. Kondou, R. Yoshimi, A. Tsukazaki, Y. Fukuma, J. Matsuno, K. S. Takahashi, M. Kawasaki, Y. Tokura, and Y. Otani, Fermi-level-dependent charge-to-spin current conversion by Dirac surface states of topological insulators, Nat. Phys. **12**, 1027 (2016).

[10] D. MacNeill, G. M. Stiehl, M. H. D. Guimaraes, R. A. Buhrman, J. Park, and D. C. Ralph, Control of spin–orbit torques through crystal symmetry in WTe_2/ferromagnet bilayers, Nat. Phys. **13**, 300 (2017).

[11] D. MacNeill, G. M. Stiehl, M. H. D. Guimarães, N. D. Reynolds, R. A. Buhrman, and D. C. Ralph, Thickness dependence of spin-orbit torques generated by WTe_2, Phys. Rev. B **96**, 054450 (2017).

[12] S. Shi, S. Liang, Z. Zhu, K. Cai, S. D. Pollard, Y. Wang, J. Wang, Q. Wang, P. He, J. Yu, G. Eda, G. Liang, and H. Yang, All-electric magnetization switching and Dzyaloshinskii-Moriya interaction in WTe_2/ferromagnet heterostructures, Nat. Nanotechnol. **14**, 945 (2019).

[13] W. Yanez, *et al.*, Spin and Charge Interconversion in Dirac-Semimetal Thin Films, Phys. Rev. Appl. **16**, 054031 (2021).

[14] H. Xu, J. Wei, H. Zhou, J. Feng, T. Xu, H. Du, C. He, Y. Huang, J. Zhang, Y. Liu, H.-C. Wu, C. Guo, X. Wang, Y. Guang, H. Wei, Y. Peng, W. Jiang, G. Yu, and X. Han, High spin Hall conductivity in large-area type-II Dirac semimetal $PtTe_2$, Adv. Mater. **32**, 2000513 (2020).

[15] B.-C. Lin, S. Wang, A.-Q. Wang, Y. Li, R.-R. Li, K. Xia, D. Yu, and Z.-M. Liao, Electric Control of Fermi Arc Spin Transport in Individual Topological Semimetal Nanowires, Phys. Rev. Lett. **124**, 116802 (2020).

[16] G. M. Stephen, A. T. Hanbicki, T. Schumann, J. T. Robinson, M. Goyal, S. Stemmer, and A. L. Friedman, Room-temperature spin transport in Cd_3As_2, ACS Nano **15**, 5459 (2021).

[17] S.-Y. Xu, *et al.*, Discovery of a Weyl fermion semimetal and topological Fermi arcs, Science **349**, 613 (2015).

[18] S.-Y. Xu, *et al.*, Spin Polarization and Texture of the Fermi Arcs in the Weyl Fermion Semimetal TaAs, Phys. Rev. Lett. **116**, 096801 (2016).

[19] Y. Sun, Y. Zhang, C. Felser, and B. Yan, Strong Intrinsic Spin Hall Effect in the TaAs Family of Weyl Semimetals, Phys. Rev. Lett. **117**, 146403 (2016).

[20] H. An, Y. Kageyama, Y. Kanno, N. Enishi, and K. Ando, Spin–torque generator engineered by natural oxidation of Cu, Nat. Commun. **7**, 13069 (2016).

[21] H. Tsai, S. Karube, K. Kondou, N. Yamaguchi, F. Ishii, and Y. Otani, Clear variation of spin splitting by changing

electron distribution at non-magnetic metal/Bi_2O_3 interfaces, Sci. Rep. **8**, 5564 (2018).

[22] N. Reyren, M. Bibes, E. Lesne, J.-M. George, C. Deranlot, S. Collin, A. Barthélémy, and H. Jaffrès, Gate-Controlled Spin Injection at $LaAlO_3/SrTiO_3$ Interfaces, Phys. Rev. Lett. **108**, 186802 (2012).

[23] P. Noël, F. Trier, L. M. Vicente Arche, J. Bréhin, D. C. Vaz, V. Garcia, S. Fusil, A. Barthélémy, L. Vila, M. Bibes, and J.-P. Attané, Non-volatile electric control of spin–charge conversion in a $SrTiO_3$ Rashba system, Nature **580**, 483 (2020).

[24] S. Ohya, D. Araki, L. D. Anh, S. Kaneta, M. Seki, H. Tabata, and M. Tanaka, Efficient intrinsic spin-to-charge current conversion in an all-epitaxial single-crystal perovskite-oxide heterostructure of $La_{0.67}Sr_{0.33}MnO_3/LaAlO_3/SrTiO_3$, Phys. Rev. Res. **2**, 012014(R) (2020).

[25] T. Tanaka, H. Kontani, M. Naito, T. Naito, D. S. Hirashima, K. Yamada, and J. Inoue, Intrinsic spin Hall effect and orbital Hall effect in 4*d* and 5*d* transition metals, Phys. Rev. B **77**, 165117 (2008).

[26] D. Go, D. Jo, T. Gao, K. Ando, S. Blügel, H.-W. Lee, and Y. Mokrousov, Orbital Rashba effect in a surface-oxidized Cu film, Phys. Rev. B **103**, L121113 (2021).

[27] I. Vurgaftman, J. R. Meyer, and L. R. Ram-Mohan, Band parameters for III–V compound semiconductors and their alloys, J. Appl. Phys. **89**, 5815 (2001).

[28] A. Bedoya-Pinto, A. K. Pandeya, D. Liu, H. Deniz, K. Chang, H. Tan, H. Han, J. Jena, I. Kostanovskiy, and S. S. P. Parkin, Realization of epitaxial NbP and TaP Weyl semimetal thin films, ACS Nano **14**, 4405 (2020).

[29] X. Huang, L. Zhao, Y. Long, P. Wang, D. Chen, Z. Yang, H. Liang, M. Xue, H. Weng, Z. Fang, X. Dai, and G. Chen, Observation of the Chiral-Anomaly-Induced Negative Magnetoresistance in 3D Weyl Semimetal TaAs, Phys. Rev. X **5**, 031023 (2015).

[30] T. M. Cham, S. Karimeddiny, V. Gupta, J. A. Mittelstaedt, and D. C. Ralph, Separation of artifacts from spin-torque ferromagnetic resonance measurements of spin-orbit torque for the low-symmetry van der Waals semi-metal $ZrTe_3$, Adv. Quantum Technol. **5**, 2100111 (2022).

[31] S. Karimeddiny, J. A. Mittelstaedt, R. A. Buhrman, and D. C. Ralph, Transverse and Longitudinal Spin-Torque Ferromagnetic Resonance for Improved Measurement of Spin-Orbit Torque, Phys. Rev. Appl. **14**, 024024 (2020).

[32] Y. Ou, C.-F. Pai, S. Shi, D. C. Ralph, and R. A. Buhrman, Origin of field-like spin-orbit torques in heavy metal/ferromagnet/oxide thin film heterostructures, Phys. Rev. B **94**, 140414(R) (2016).

[33] D. Zhu, Y. Wang, S. Shi, K.-L. Teo, Y. Wu, and H. Yang, Highly efficient charge-to-spin conversion from *in situ* Bi_2Se_3/Fe heterostructures, Appl. Phys. Lett. **118**, 062403 (2021).

[34] A. Bose, J. N. Nelson, X. S. Zhang, P. Jadaun, R. Jain, D. G. Schlom, D. C. Ralph, D. A. Muller, K. M. Shen, and R. A. Buhrman, Effects of anisotropic strain on spin–orbit torque produced by the Dirac nodal line semimetal IrO_2, ACS Appl. Mater. Interfaces **12**, 55411 (2020).

[35] D. Lee, W. Jeong, D. Yun, S.-Y. Park, B.-K. Ju, K.-J. Lee, B.-C. Min, H. C. Koo, and O. Lee, Effects of interfacial oxidization on magnetic damping and spin–orbit torques, ACS Appl. Mater. Interfaces **13**, 19414 (2021).

[36] Y. Fan, H. Li, M. DC, T. Peterson, J. Held, P. Sahu, J. Chen, D. Zhang, A. Mkhoyan, and J.-P. Wang, Spin pumping and large field-like torque at room temperature in sputtered amorphous WTe_{2-x} films, APL Mater. **8**, 041102 (2020).

[37] M. DC, R. Grassi, J.-Y. Chen, M. Jamali, D. Reifsnyder Hickey, D. Zhang, Z. Zhao, H. Li, P. Quarterman, Y. Lv, M. Li, A. Manchon, K. A. Mkhoyan, T. Low, and J.-P. Wang, Room-temperature high spin–orbit torque due to quantum confinement in sputtered $Bi_xSe_{(1-x)}$ films, Nat. Mater. **17**, 800 (2018).